journal

J. Am. Ceram. Soc., **90** [1] 199–204 (2007)
DOI: 10.1111/j.1551-2916.2006.01381.x

Modeling the Influence of Orientation Texture on the Strength of WC–Co Composites

Chang-Soo Kim*,†

Department of Materials Science and Engineering, Carnegie Mellon University, Pittsburgh, Pennsylvania 15213

Ted R. Massa

Kennametal Incorporated, Corporate Technology, 1600 Technology Way, P.O. Box 231, Latrobe, Pennsylvania 15650

Gregory S. Rohrer*,‡

Department of Materials Science and Engineering, Carnegie Mellon University, Pittsburgh, Pennsylvania 15213

Two-dimensional finite element simulations were used to study the effects of orientation texture on the transverse rupture strengths of WC–Co composites. The model incorporates observed microstructural geometries, anisotropic thermal and elastic properties, and a fracture criterion that reproduces the strengths of known specimens. The results show that the greatest potential for increasing the strength occurs when the [001] axes of the carbide grains are orientated perpendicular to the sample loading direction. Furthermore, the strength increases in proportion to the degree of texture, and the texture-derived strength enhancement is greater in microstructures with a larger contiguity.

I. Introduction

Tungsten carbide-cobalt (WC-Co) composites are widely used in manufacturing processes that benefit from their combination of high hardness, fracture toughness, strength, and wear resistance. Like other engineering materials, it is well known that the microstructural characteristics of these composites strongly influence their mechanical properties. In particular, the grain size and volume fraction of the carbide phase are the primary factors that influence mechanical properties.[1–3] Recently, a two-dimensional finite element model has been used to independently simulate the effects of carbide contiguity, angularity, shape, and size distribution on the strength.[4] This work led to the conclusion that for samples of constant grain size and carbide volume fraction, the most important factor is the contiguity of the carbide skeleton. The results showed that as the contiguity increases, higher stresses are concentrated in the carbide phase and that this is detrimental to the strength. The angularity of the carbide crystal, the aspect ratio, and the crystal size distribution all have smaller effects on strength. In general, low angularity, high WC aspect ratios, and a wider crystal size distribution are detrimental to fracture strength. Other mechanical properties, such as fracture toughness, are not necessarily expected to follow the same trends. In all of the cases studied previously, randomly textured materials were simulated. The purpose of the current paper is to describe the influence of grain orientation texture on the strength of WC–Co composites.

To simulate the residual stress distributions and strengths of real and hypothetical microstructures, we use the object oriented finite (OOF) element code developed by the National Institute of Standards and Technology (NIST, Gaithersburg, MD).[5] OOF is designed to approximate solutions in stress–strain states of complex microstructures (including a large number of grains) under mechanical and/or thermal loads. Previously, this code has been used to calculate the residual stress and elastic energy density (EED) distributions in textured and non-textured polycrystalline alumina.[6] In that case, texturing decreased the residual stress and stored energy. OOF has been used to study thermal expansion-induced spontaneous microcracking in alumina.[7] The OOF package has also been used to calculate Young's moduli and thermal expansion coefficients of silicon carbide–aluminum (SiC–Al) and double carbide (WC–Co) composites.[8–10] More advanced models have recently been used to calculate the mechanical properties of metal–ceramic composites, but crystallographic properties have not been incorporated into these simulations.[11–12]

The methods used in the present paper to simulate the residual stresses and strengths of textured WC–Co composites have already been described in detail.[4] Briefly, a brittle fracture criterion is used to determine the stress at which the model fails. This fracture criterion is based on a fracture energy set to minimize the difference between the calculated and experimentally measured strengths of four specimens with a range of different microstructural characteristics. Using this model, experimental elastic moduli were reproduced within 2% and experimental transverse rupture strengths were reproduced within 6%. In the current paper, the same model is used to study the effect of orientation texture.

II. Methods

The hypothetical microstructures described in this paper were derived from the microstructures of four conventional WC–Co composites with no intentionally added impurities. The samples were consolidated by liquid-phase sintering for approximately 45 min at 1400°–1600°C (lower temperatures were used for materials with more Co). After sintering, the samples were polished using a diamond abrasive and etched in Murakami's reagent (10 g potassium ferricyanide and 10 g sodium hydroxide added to 100 mL distilled water) for 1 min. The reagent preferentially etches the WC grains depending on their crystallographic orientations, which leads to sharp contrast differences in AFM images (see Fig. 1(a)). The orientations of the WC crystals were measured using an automated electron-backscattered diffraction mapping system (EDAX Inc., Draper, UT) combined with a Philips XL 40 scanning electron microscope (Philips Electronic Instruments, Mahwah, NJ). The orientation maps were record-

K. Bowman—contributing editor

Manuscript No. 21654. Recevied March 31, 2006; approved September 23, 2006.

This work was supported primarily by Kennametal Incorporated and the Pennsylvania Technology Infrastructure Authority. Partial support by the MRSEC program of the National Science Foundation under Award Number DMR-0520425 is also acknowledged.

*Member, American Ceramic Society.

†Current address: Division of Chemistry and Materials Science, U.S. Food and Drug Administration, Rockville, MD 20852.

‡Author to whom correspondence should be addressed. e-mail: gr20@andrew.cmu.edu

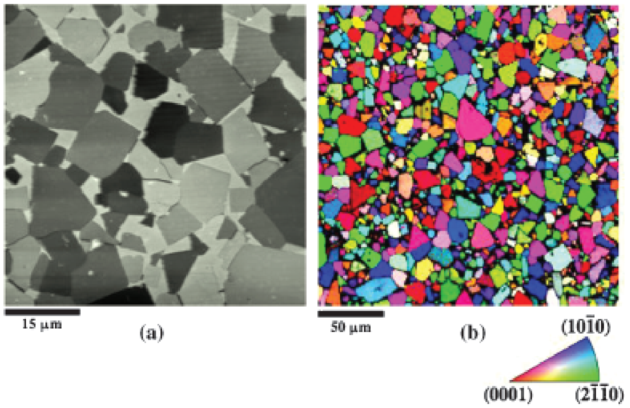

Fig. 1. Example of (a) AFM topography map and (b) inverse pole figure (IPF) map derived from electron backscatter diffraction mapping (of sample A). The Co phase was not indexed in the IPF map and appears black.

ed with a 0.2–1.0 μm step size (the larger step size was used for the sample with the largest grain size) and processed as previously described to remove spurious orientations and to obtain an average orientation for each grain.[13] The AFM and orientation data were analyzed to determine the average carbide grain sizes and the contiguity of the carbide phase (see Table I).[4] To determine the contiguity, the positions of binder/carbide interfaces and carbide/carbide boundaries in AFM images were manually traced using a computer program that uses the position of the computer's mouse to automatically record the vector components of binder/carbide (l_{bc}) and carbide/carbide (l_{cc}) line segments. Approximately 2500 grains in each specimen were analyzed. The contiguity was then calculated according to the following equation:

$$C = \frac{2\sum_i l^i_{cc}}{\sum_{i,j}(2l^i_{cc} + l^j_{bc})} \tag{1}$$

The samples possessed no obvious orientation texture; this is clear from the inverse pole figure map of sample A shown in Fig. 1(b). The maximum value in the orientation distribution function (ODF) derived from the orientation maps is 1.6 multiples of a random distribution (MRD).

To create textured microstructures, we begin by defining the probability (p) of finding a crystal whose orientation places a certain axis in the crystal frame ($\langle 100\rangle$, $\langle 111\rangle$, or $\langle 001\rangle$) Δ degrees away from a specific sample axis, [100], [111], or [001], according to the following equation:

$$p = \exp(-\Delta/\beta) \tag{2}$$

The relationship between the sample and crystal reference frame is shown schematically in Fig. 2(a), and β is a constant that determines the intensity (or degree) of orientation texture. We used $\beta = 2$, 10, and 25 to construct qualitatively high, medium, and low orientation-textured microstructures, respectively. The maxima in the ODFs of the high-, medium-, and low-texture samples are 11.8, 3.7, and 2.0 MRD, respectively. These values represent an average over an orientation range of 5° about the maximum. The probabilities given by Eq. (2) for the three different textures are compared in Fig. 2(b). It is clear that in the high-texture case ($\beta = 2$), the probability of finding a crystal with a deviation angle (Δ) greater than 10° is nearly zero.

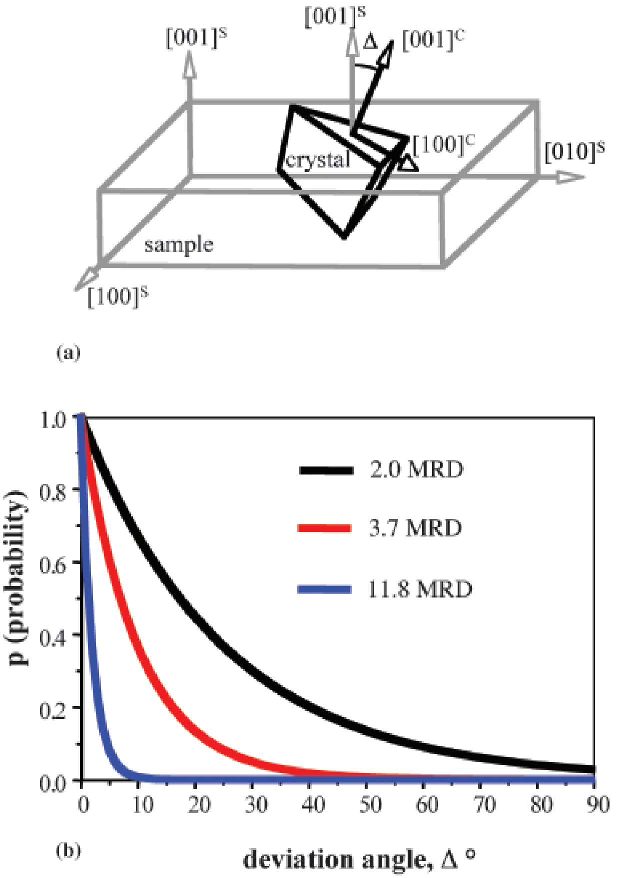

Fig. 2. (a) Schematic illustration of the sample and crystal reference frames showing the deviation angle (Δ) between the $[001]^S$ sample axis and a $\langle 001\rangle^C$ crystal axis. The sample and crystal axes are labeled with the superscripts S and C, respectively. (b) Probability of finding a crystal with an orientation as a function of the deviation angle (Δ) from a sample axis for three different texture intensity factors.

To develop microstructures that have the textures defined by Eq. (2), orientations were assigned to the crystals in the observed micrographs according to the following algorithm. First, a random set of three Euler angles is selected and the angle Δ between a certain crystal axis and a fixed sample axis is calculated. According to Eq. (2), this defines a probability between zero and one. Another random number is then selected, also between zero and one, and compared with the probability defined by Δ. If the random number is less than the probability computed from Δ and a predefined value of β, the Euler angles are accepted and, otherwise, they are discarded. The process is repeated until the orientations of all of the carbide crystals are assigned. Using this method, hypothetical microstructures with $(001)^C//[001]^S$, $(100)^C//[100]^S$, and $(111)^C//[111]^S$ orientation textures were created, where the superscript C denotes the crystal reference frame and the superscript S denotes the sample reference frame. For brevity, the three textures are referred to as [001], [100], and [111].

Table I. Measured Microstructural Features and Transverse Rupture Strength (TRS) for the Four Samples

Sample	$\bar{d}$ (μm)	λ (μm)	f_c	C	TRS (GPa)
A	5.31 (3.19)	1.72 (1.35)	0.885	0.595	1.94 (0.05)
B	1.65 (0.97)	0.53 (0.39)	0.885	0.591	3.29 (0.13)
C	1.41 (0.90)	0.63 (0.48)	0.822	0.501	2.84 (N/A)
D	1.40 (0.88)	0.96 (0.81)	0.692	0.351	2.57 (N/A)

$\bar{d}$ is the average WC diameter, λ is the binder mean free path, f_c is the WC volume fraction, C is the contiguity, and TRS is the transverse rupture strength, respectively. The values in parentheses are standard deviations.

Table II. (a) Elastic Constants and (b) Coefficients of Thermal Expansion of the WC and Co Phases[16–18]

	WC	Co
(a)		
C_{11} (GPa)	720	
C_{33} (GPa)	972	
C_{44} (GPa)	328	
C_{12} (GPa)	254	
C_{13} (GPa)	267	
E (GPa)	714	211
ν	0.19	0.31
(b)		
α_{11} K^{-1}	5.2×10^{-6}	
α_{33} K^{-1}	7.3×10^{-6}	
α K^{-1}		1.4×10^{-5}

C_{11}–C_{13} are the stiffness of WC, E is the bulk Young's modulus, ν is the Poisson's ratio of WC and Co, α_{11}, and α_{33} are the anisotropic coefficients of thermal expansion of WC, and α is the isotropic coefficient of the thermal expansion of Co.

It should be pointed out that the method we use to simulate the textured microstructures neglects the geometric constraints that relate the crystal shapes to orientations. It is well known that the WC crystal shapes in WC–Co composites are trigonal prisms or truncated trigonal prisms.[13–15] For example, grains with their $\langle 001\rangle$ axis parallel to the [001] sample axis (those appearing red in Fig. 1(b)) are nearly always triangular. In the simulations described here, this correlation is ignored.

Each computational section (containing 600–900 WC crystals) was cropped from a much larger orientation map (see Fig. 1(b)). Table II shows the elastic constants and the coefficients of thermal expansion (CTE) that were used in the simulations.[16–18] The anisotropic thermoelastic properties of WC were included in the simulations but, because the orientations of the crystals in the binder phase were not determined, the Co was modeled as isotropic. It turns out, however, that the isotropic assumption for Co does not alter the results significantly. Tests using random assignments of Co orientations and actual stiffnesses yielded the same results as tests using isotropic elastic constants. The consistency of the results from the two elastic models derives from the fact that the residual stresses are concentrated in the stiffer carbide phase. After assigning orientations and physical properties, computational sections were discretized into 1.8×10^5–2.1×10^5 finite elements.

In the simulations, we assume a brittle (Griffith like) fracture process. In other words, the stress at the point where the EED exceeds the critical threshold is taken as the fracture strength[5]

$$2\gamma\Delta L \leq \frac{1}{2}\sigma_{ij}\varepsilon_{ij}A \qquad (3)$$

where γ is the surface energy of the cracked interface, ΔL is the edge length, A is the area, σ_{ij} is the stress, and ε_{ij} is the strain of an element, respectively. Although the actual fracture process in WC–Co composites is believed to involve considerable plastic deformation of the binder phase, we assume a linear stress–strain behavior before failure. This brittle fracture assumption is supported by the experimental TRS test data. Östberg *et al.*[19,20] reported that the stress exhibits an almost linear behavior with applied strain until failure during TRS tests below 800°C. We also assume that failure occurs only in the carbide phase: transgranular in the carbide crystal or intergranular along carbide crystals. Although it is recognized that there are four possible crack paths (intergranular along WC/WC boundaries, intergranular along WC/Co interfaces, transgranular in WC crystals, and transgranular in the Co), this assumption is consistent with the theoretical fracture energy models of Sigl and Fischmeisters.[21] They surmised that the fracture energies of the WC phase are significantly lower than those of the WC/Co interface and/or the Co phase. Furthermore, we assume that the fracture energy in the carbide phase is a constant independent of the two primary microstructural parameters: grain size and volume fraction of the WC phase. Because it is not feasible to obtain the correct fracture energy (γ) distributions as a function of crystallographic orientation and/or misorientation in the WC phase, we determined an effective γ that represents the whole fracture process by comparing calculated fracture strengths and experimentally measured values. The procedure for obtaining the value used in this paper ($\gamma = 49$ J/m^2) is described completely elsewhere.[4]

The simulations in this work were performed under plane-stress and fixed boundary conditions (the displacement of the surface perpendicular to the loading direction is fixed). The elastic modulus was calculated by averaging the stress in each element at an imposed strain of 0.0001. To calculate the fracture strength, a combined mechanical and thermal load was applied. Because the materials are sintered at 1400°–1600°C, a cooling temperature of $\Delta T = -1400$°C was used as a thermal load.

III. Results

The calculated composite moduli of the hypothetical-textured microstructures derived from sample A are plotted in Fig. 3. There are nine distinct models, three (high, medium, and low) [001] textures, three [100] textures, and three [111] textures. In Fig. 3, the moduli of the [001] and [111] textured samples were calculated by averaging the results from simulations with elongations along the $[100]^S$ and $[010]^S$ directions. However, because of the elastic anisotropy of WC, the modulus of the [100] textured sample was considered separately along the $[100]^S$ and $[010]^S$ directions. Note that the stiffness along the c axis (C_{33}) in WC is much higher than other directions (see Table II), and this direction is preferentially aligned along the $[010]^S$ direction of the sample reference frame. This explains why the modulus of the [100] textured sample is higher in the $[010]^S$ direction than in the $[100]^S$ direction.

The dotted horizontal line in Fig. 3 denotes the experimentally measured modulus of the material with no orientation texture. It is clear that as the degree of texture decreases (the maximum of the ODF decreases from 11.8 to 2.0 MRD), the calculated modulus approaches the value measured for the randomly textured material. The modulus of the [001] textured sample is always lower than the measured value for the randomly textured material as the stiffest axis (c axis) is not aligned along the direction of elongation. In the case of the [100] textured sample, the modulus along the c-axis direction ($[010]^S$) is

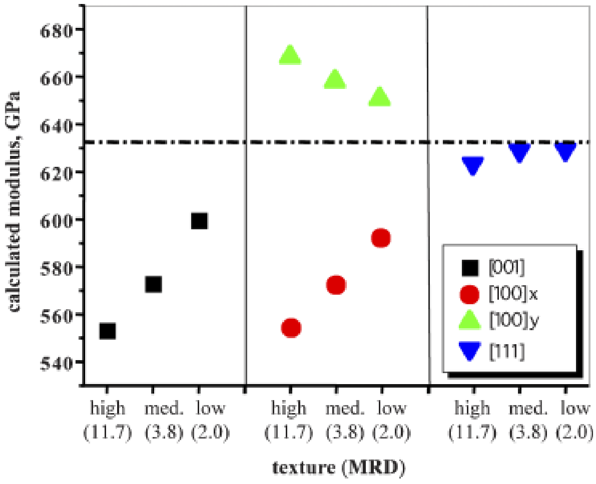

Fig. 3. Calculated modulus for samples with [001], [100], and [111] orientation textures. The dotted line indicates the experimentally measured modulus of an untextured sample. As the sample becomes less textured (the multiples of a random distribution [MRD] value decreases), the calculated modulus approaches the measured value for the untextured material. In the legend, x denotes elongation in the $[100]^S$ direction and y denotes elongation in the $[010]^S$ direction.

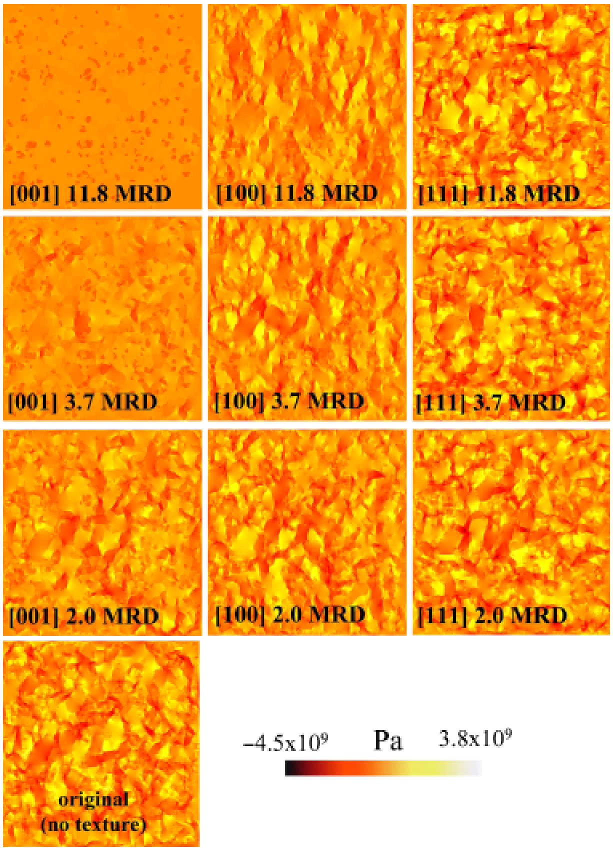

Fig. 4. Thermal stress (SI1) distributions for samples with different orientation textures after cooling 1400°C. The same scale is used for each figure. The label in each panel indicates the type of texture and the peak value of the orientation distribution functions.

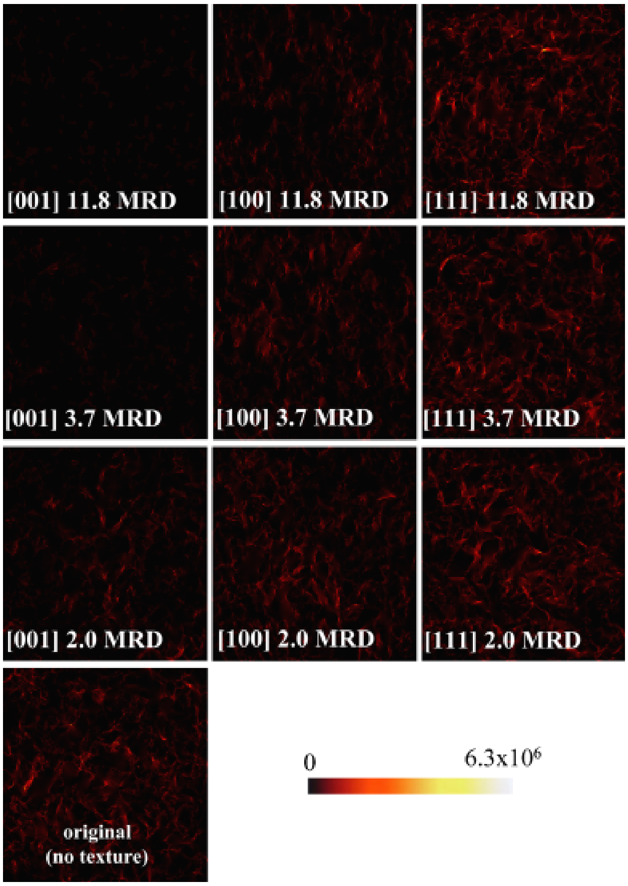

Fig. 5. Elastic energy density distributions for samples with different orientation textures after cooling 1400°C. The same scale is used for each figure.

invariably higher than the modulus of the randomly textured material, and the modulus along the direction perpendicular to the *c* axis ($[100]^S$) is lower than the randomly textured value. The modulus of sample with [111] texture is nearly the same as the measured quantity, which means that the response is almost isotropic along the $[100]^S$ and $[010]^S$ directions of the sample reference frame.

The stress invariant 1 ($\sigma_{11}+\sigma_{22}+\sigma_{33}$, hydrostatic stress, hereafter SI1) and EED ($0.5\Sigma(\sigma_{ij}\times\varepsilon_{ij})$) were then computed for these hypothetical microstructures. To reveal the texture effect clearly, the simulations in Figs. 4 and 5 were subjected to only a thermal load of $\Delta T=-1400°C$ under free and plane-stress boundary conditions. The same scales were used for SI1 and EED to visualize the relative distributions. The distributions in the real microstructure (no orientation texture) are illustrated in the lower left-hand corners of Figs. 4 and 5. It is apparent that the sample with a high [001] texture shows reduced stresses and EEDS. As the intensity of the texture decreases, the stress and energy distributions resemble the original distributions.

The fracture strength was calculated under a combined thermal and mechanical load in six of the nine sections (three with [001] texture and three with [100] texture, from sample A). Simulations were carried out under the same conditions as in the real microstructure (plane-stress and fixed boundary conditions, and $\Delta T=-1400°C$). The cases where the most compliant axis is along the loading direction ([001] texture) and where the least compliant axis is in the loading direction ([100] texture loaded along $[010]^S$) bound the range of responses, and these results are presented in Fig. 6. Note that the strength of the [001] textured sample is the average of results from elongation in the $[100]^S$ and $[010]^S$ directions and the strength of the [100] textured sample was obtained by elongation in $[010]^S$. The results show that the [001] textured samples clearly have a higher strength; the dotted line indicates the calculated strength of the untextured material (1.83 GPa). Even in the calculations with stress parallel to the stiffest axis ($[010]^S$ direction of [100] texture), the calculated strength is not worse than that of the real microstructure. The result indicates that the strength can be potentially increased between 2% and 13% by texturing the sample.

To generalize the results derived from sample A, we expand the calculation to other specimens (B, C, and D). Three different sections have been analyzed for each microstructure. The calculated fracture strength increase (%) is given in Fig. 7A. The results are based on 72 independent simulations (there were four

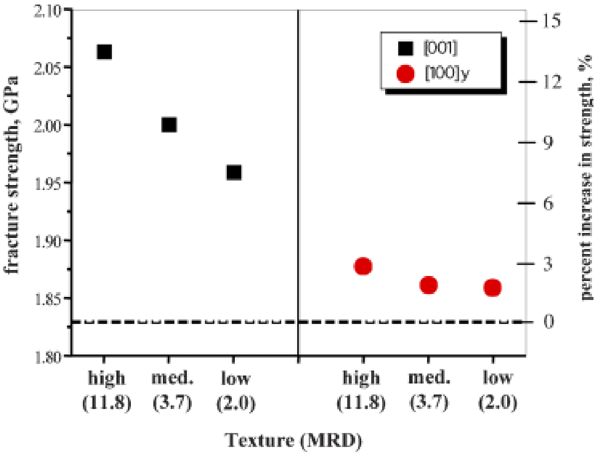

Fig. 6. Calculated fracture strength (left ordinate) and fracture strength increase (right ordinate) for [001] and [100] orientation textures. The dotted line represents the calculated strength of the real microstructure with no texture.

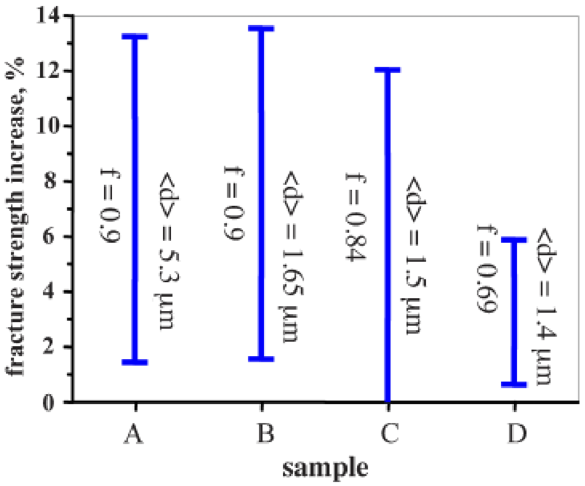

Fig. 7. Calculated fracture strength increase for hypothetical microstructures. The bars for each sample show the range of calculated strength increase for different textures and sections.

different specimens, six different textures for each specimen, and three different sections for each case). The range of the calculated fracture strength increase was calculated to be −2% to 13%. For all of the microstructures, the maximum strength was found in the highly textured [001] samples, and the minimum strength was found in the $[010]^S$ direction of highly textured [100] samples. In the $[010]^S$ direction of the highly textured [100] sample, the calculated strength was sometimes lower than that of the real sample; note that the minimum change in specimen C is −2%. Thus, although orientation texture usually increases the strength along a certain direction, there are also cases where the strength is reduced. It was found that the relative maximum increment of the strength for different specimens is linear with the contiguity of the samples (see Fig. 8).

IV. Discussion

There are two mechanisms by which texture influences the strength of WC–Co composites. The first is that as the degree of alignment of the carbide crystals increases, the thermal expansion incompatibilities that arise during cooling are minimized. As a result, the residual stresses are decreased and this contributes to the increased strength of the material. The second mechanism is related to elastic anisotropy of the carbide. The carbide crystals are more compliant in the directions perpendicular to the [001] axis. Therefore, when these more compliant directions are aligned along the direction of elongation, the stresses that develop are lower than for an average orientation and this leads to greater strength.

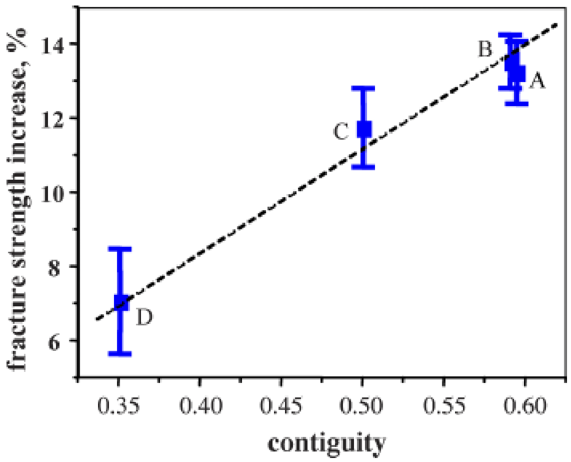

Fig. 8. Calculated maximum fracture strength increase for each grade as a function of contiguity. Error bars indicate the standard deviation in the calculated result using different sections of each sample.

We also find that the strength enhancement increases with the contiguity of the carbide. To avoid confusion, we should note that the texture-induced strength enhancement within separate specimens is not necessarily correlated to the comparative strength of different specimens. For example, for two untextured composites with the same composition and grain size, but different contiguity, we expect the low-contiguity specimen to be stronger. If the two specimens are then textured by the same amount, the fractional increase in strength will be greater in the high-contiguity sample, even though the absolute strength of this sample might be less than the low-contiguity sample. The reasons for this are that as the contiguity of the carbide network increases, the thermal expansion mismatches between the carbide grains increase. This leads to greater residual stresses. The textured alignment of the carbide crystals reduces thermal expansion mismatches. Because the reduction of thermal mismatch is more pronounced in high-contiguity composites, the strength enhancement is greater. It should be noted that this conclusion is probably dependent on the validity of the so-called "skeletonized carbide" hypothesis that we have adopted in this work.[22] In other words, we assume that there is a contiguous carbide phase throughout the microstructure. This assumption is supported by transmission electron microscopic studies that conclude that there are direct carbide-to-carbide transitions at the grain boundaries.[23] However, it has been reported that carbide/carbide grain boundaries always contain Co as a submonolayer segregant and this has led some to propose a "dispersed carbide" model that assumes that the carbide crystals are dispersed in a continuous binder phase.[24,25] In the calculations described here, it is assumed that even if a small amount of Co is present at the grain boundaries between carbide crystals, the boundaries remain brittle and are more nearly like the bulk carbide phase than the bulk Co phase.

It is likely that the strength might be further enhanced by also controlling the distributions of grain boundary misorientations. Calculations of thermally anisotropic polycrystals have recently demonstrated that changing the distribution of grain boundary misorientations (while the grain orientation distribution is constant) can significantly reduce the residual stresses.[26] By analogy with the calculations described here, reduced residual stresses should lead to increased strength. As a general result, increasing the number of low misorientation angle grain boundaries reduces the residual stresses.

In addition to orientation and misorientation textures, the distribution of grain boundary planes can also influence residual stresses.[26] As mentioned in Section II, we have not accounted for the correlation between the grain orientation and the trigonal prismatic shapes of the carbide grains. However, in an earlier study that did consider the effect of shape on strength, and used the same model as the current work, it was found that when circular and triangular carbide grains were compared, there was only a 3% difference in strength.[4] Therefore, shape is not expected to influence strength more than texture. In fact, if we compare the current results with the conclusions in Kim *et al.*,[4] we can summarize in the following way. The most important aspects of the microstructure are the grain size and the carbide volume fraction. Texture and contiguity are the next most influential. Angularity, shape, aspect ratio, and grain size distribution are all subordinate parameters. If these predictions are accurate and the increases in strength are additive, then it can be concluded that for a fixed grain size and carbide volume fraction, WC–Co composites with low contiguity, a high degree of orientation texture, equiaxed, angular carbide crystal shapes, and a uniform carbide grain size distribution will display the optimum fracture strength.

V. Conclusion

We have used a two-dimensional finite element model to compute the strengths of hypothetical WC–Co composites with a range of different microstructures and orientation textures. The results show that the greatest potential for increasing the strength occurs when the [001] axes of the carbide grains are orientated perpendicular to the sample loading direction. Furthermore, the strength increases in proportion to the degree of texture and the strength enhancement deriving from the texture is greater in microstructures with a larger contiguity.

Acknowledgments

The authors thank E. R. Fuller, Jr. (NIST) and D. M. Saylor (USFDA) for their advice and help with this work.

References

[1] J. Gurland, "New Scientific Approaches to the Development of Tool Materials," *Int. Mater. Rev*., **33** [3] 151–66 (1988).

[2] X. Deng, B. R. Patterson, K. K. Chawla, M. C. Koopman, C. Mackin, Z. Fang, G. Lockwood, and A. Griffo, "Microstructure/Hardness Relationship in a Dual Composite," *J. Mater. Sci. Lett*., **21** [9] 707–9 (2002).

[3] X. Deng, B. R. Patterson, K. K. Chawla, M. C. Koopman, Z. Fang, G. Lockwood, and A. Griffo, "Mechanical Properties of a Hybrid Cemented Carbide Composite," *Int. J. Ref. Metals. Hard. Mater*., **19** [4–6] 547–52 (2001).

[4] C.-S. Kim, T. R. Massa, and G. S. Rohrer, "Modeling the Relationship Between Microstructural Features and the Strength of WC–Co Composites," *Int. J. Ref. Metals. Hard. Mater*., **24** [1–2] 89–100 (2006).

[5] W. C. Carter, S. A. Langer, and E. R. Fuller Jr. The OOF Manual. version 1.0.8.6. National Institute of Standards and Technology (NIST); 2001, also available online at http://www.ctcms.nist.gov/oof.

[6] V. R. Vedula, S. J. Glass, D. M. Saylor, G. S. Rohrer, W. C. Carter, S. A. Langer, and E. R. Fuller, "Residual-Stress Predictions in Polycrystalline Alumina," *J. Am. Ceram. Soc*., **84** [12] 2947–54 (2001).

[7] G. Galal Yousef, J. Rödel, E. R. Fuller Jr., A. Zimmerman, and B. S. El-Dasher, "Microcrack Evolution in Alumina Ceramics: Experiment and Simulation," *J. Am. Ceram. Soc*., **88** [10] 2809–16 (2005).

[8] N. Chawla, B. V. Patel, M. Koopman, K. K. Chawla, R. Saha, B. R. Patterson, E. R. Fuller, and S. A. Langer, "Microstructure-Based Simulation of Thermomechanical Behavior of Composite Materials by Object-Oriented Finite Element Analysis," *Mater. Character*., **49** [5] 395–407 (2002).

[9] M. Koopman, K. K. Chawla, C. Coffin, B. R. Patterson, X. Deng, B. V. Patel, Z. Fang, and G. Lockwood, "Determination of Elastic Constants in WC/Co Metal Matrix Composites by Resonant Ultrasound Spectroscopy and Impulse Excitation," *Adv. Eng. Mater*., **4** [1–2] 37–42 (2002).

[10] N. Chawla and K. K. Chawla, "Microstructure-Based Modeling of the Deformation Behavior of Particle Reinforced Metal Matrix Composites," *J. Mater. Sci*., **41** [3] 913–25 (2006).

[11] N. Chawla, R. S. Sidhu, and V. V. Ganesh, "Three-Dimensional Visualization and Micro Structure-Based Modeling of Deformation in Particle-Reinforced Composites," *Acta Mater*., **54** [6] 1541–8 (2006).

[12] V. V. Ganesh and N. Chawla, "Effect of Particle Orientation Anisotropy on the Tensile Behavior of Metal Matrix Composites: Experiments and Micro Structure-Based Simulation," *Mater. Sci. Eng. A*, **391** [1-2] 342–52 (2005).

[13] C.-S. Kim and G. S. Rohrer, "Geometric and Crystallographic Characterization of WC Surfaces and Grain Boundaries in WC–Co Composites," *Interface Sci*., **12** [1] 19–27 (2004).

[14] A. V. Shatov, S. A. Firstov, and I. V. Shatova, "The Shape of WC Crystals in Cemented Carbides," *Mater. Sci. Eng. A*, **242** [1–2] 7–14 (1998).

[15] S. Kim, S.-H. Han, J.-K. Park, and H.-E. Kim, "Variation of WC Grain Shape with Carbon Content in the WC–Co Alloys During Liquid-Phase Sintering," *Scripta Mater*., **48** [5] 635–9 (2003).

[16] M. Lee and R. S. Gilmore, "Single Crystal Elastic Constants of Tungsten Monocarbide," *J Mater. Sci*., **17** [9] 2657–60 (1982).

[17] A. Kelly and G. W. Groves, *Crystallography and Crystal Defects*. Longman, London, 1973.

[18] W. M. Stoll and A. T. Santhanam, *Kirk-Othmer Encyclopedia of Chemical Technology*, 4th edition, John Wiley and Sons, 1992, p. 861.

[19] G. Östberg, K. Buss, M. Christensen, S. Norgren, H.-O. Andrén, D. Mari, G. Wahnström, and I. Reineck, "Effect of TaC on Plastic Deformation of WC–Co and Ti(C, N)–WC–Co," *Int. J. Ref. Metals. Hard. Mater*., **24** [1-2] 145–54 (2006).

[20] G. Östberg, K. Buss, M. Christensen, S. Norgren, H.-O. Andrén, D. Mari, G. Wahnström, and I. Reineck, "Mechanisms of Plastic Deformation of WC–Co and Ti(C,N)–WC–Co," *Int. J. Ref. Metals Hard. Mater*., **24** [1–2] 135–44 (2006).

[21] L. S. Sigl and H. F. Fischmeister, "On the Fracture Toughness of Cemented Carbides," *Acta Metall*., **36** [4] 887–97 (1988).

[22] S. Bartolucci and H. H. Schlössin, "Plastic Deformation Preceding Fracture in Tungsten Carbide–Cobalt Alloys," *Acta Metall. Mater*., **14** [3] 337–9 (1966).

[23] S. Hagege, G. Nouet, and P. Delavignette, "Grain Boundary Analysis in TEM. 4. Coincidence and the Associated Defect Structure in Tungsten Carbide," *Phys. Stat. Sol. A*, **62** [1] 97–107 (1980).

[24] A. Henjered, M. Hellsing, H.-O. Andren, and H. Norden, "Quantitative Microanalysis of Carbide/Carbide Interfaces in WC–Co-Base Cemented Carbides," *Mater. Sci. Technol*., **2** [8] 847–55 (1986).

[25] J. Gurland and J. T. Norton, "Role of the Binder Phase in the Cemented Carbide-Cobalt Alloys," *Trans. Metall. Soc. AIME*, **194** [10] 1051–56 (1952).

[26] C. S. Kim, A. D. Rollett, and G. S. Rohrer, "Grain Boundary Planes: New Dimensions in the Grain Boundary Character Distribution," *Scripta Mater*., **54** [6] 1005–9 (2006). □